J Adv Ceram

Research Article

Origins of heat and luminous saturation in LuAG:Ce thin films for high-power laser lighting

Bingguo Xue[1], Shaohong Liu[1,2,✉], Huiying Hu[1], Limin Zhou[2], Hao Cui[2], Hongying Pei[3], Wenyan Zhou[3], Manmen Liu[2,3], Haigang Dong[2], Ming Wen[2], Li Chen[2], Wei Wang[1], Song Li[1], Liang Zuo[1]

Cite this article: Xue B, Liu S, Hu H, et al. *J Adv Ceram* 2026, **15**(2): 9221238. https://doi.org/10.26599/JAC.2026.9221238

ABSTRACT: The performance of high-power laser-driven lighting systems is fundamentally limited by an insufficient understanding of the mechanisms governing heat generation and luminous saturation in color-converting materials. In this study, Ce-doped $Lu_3Al_5O_{12}$ (LuAG:Ce) thin films synthesized through spray pyrolysis across a doping range of 0.1–4.0 mol% are systematically investigated to elucidate these effects. Heat generation, resulting from the Stokes shift, is found to scale with both Ce concentration and excitation power density, emerging as a critical factor that constrains luminescence output. At an optimized doping level of 2.5 mol% Ce, the films achieve a luminous flux of 1618.3 lm and exhibit a saturation threshold of 28 W·mm^{-2} under ambient conditions. Incorporation of water cooling reduces the local laser spot temperature by approximately 42.3 °C at the same excitation intensity, effectively raising the saturation threshold to 32 W·mm^{-2} and increasing luminous flux to 1938.6 lm, representing a 19.8% enhancement. These results demonstrate that nonradiative transitions, arising from thermal quenching, lead to luminous saturation. Collectively, this study clarifies the origins of heat generation and luminous saturation in LuAG:Ce films under high-power laser excitation and underscores the critical roles of Ce doping optimization and heat dissipation in enhancing solid-state lighting performance.

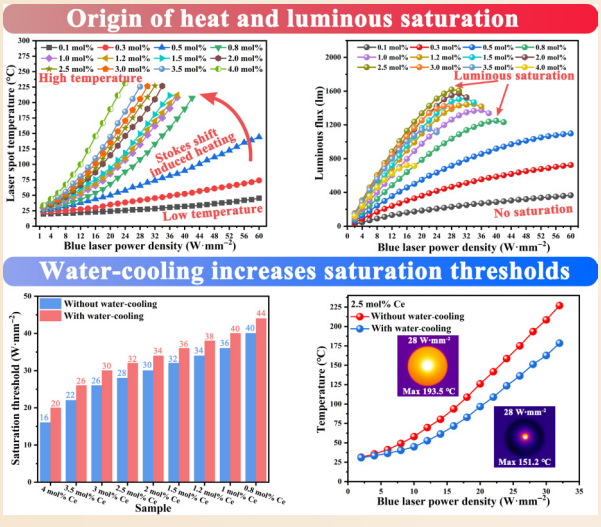

KEYWORDS: laser-driven lighting; $Lu_3Al_5O_{12}$ (LuAG:Ce) thin film; spray pyrolysis; heat generation; luminous saturation

1 Introduction

The ongoing advancement of solid-state lighting technologies prioritizes improvements in luminous efficacy, brightness, and device miniaturization. In this context, laser diodes (LDs) have emerged as superior alternatives to conventional light-emitting diodes (LEDs), offering significantly enhanced brightness and energy efficiency [1–4]. Among laser-excitable phosphor materials, Ce-doped lutetium aluminum garnet ($Lu_3Al_5O_{12}$:Ce or LuAG:Ce) is distinguished by its high quantum efficiency, strong thermal robustness, and resistance to thermal quenching [5–7]. When fabricated as thin films, LuAG:Ce offers additional performance advantages, including improved heat dissipation when integrated with thermally conductive substrates, making it an attractive candidate for high-power laser lighting applications [8–11].

A key challenge in the development of such systems is luminous saturation in the phosphor converter, wherein the emission output ceases to increase and may even decline with rising excitation power density [12–14]. This saturation effect imposes a fundamental limit on the achievable luminous flux and necessitates a detailed understanding of the mechanisms responsible for performance degradation under high-power excitation.

Luminous saturation arises from two distinct yet interdependent processes: optical saturation and thermal saturation [15–18]. Optical saturation is primarily governed by excitation intensity and activator concentration and is relatively well characterized in prior work [19–21]. In contrast, thermal saturation, driven by high temperature, presents a more complex challenge. The origin of heat generation within the phosphor matrix remains insufficiently elucidated.

[1] School of Materials Science and Engineering, Northeastern University, Shenyang 110819, China. [2] State Key Laboratory of Precious Metal Functional Materials, Yunnan Precious Metals Laboratory Co., Ltd., Kunming 650106, China. [3] Sino-Platinum Metals Semiconductor Materials (Yunnan) Co., Ltd., Kunming 650106, China.

✉ Corresponding author. E-mail: S. Liu, liush@smm.neu.edu.cn

Received: July 26, 2025; Revised: December 22, 2025; Accepted: January 3, 2026

Evidence from Ce-doped garnet systems suggests that elevated Ce concentrations accelerate heat generation and reduce the thermal saturation threshold [22,23]. For example, Xu *et al.* [24] demonstrated that increasing Ce content in $Y_{3-x}Al_5O_{12}:Ce_x$ ceramics exacerbates thermal effects under high excitation, while similar phenomena have been observed in YAG:Ce single crystals [25] and LuAG:Ce transparent ceramics [26]. These studies highlight the pivotal role of thermal processes in emission degradation; however, existing analyses offer limited insight into the underlying heat generation mechanisms and their direct influence on luminous saturation [27,28]. Moreover, the dependence of saturation characteristics on Ce concentration and the potential shift in dominant mechanisms across low and high Ce contents remain unexplored.

To address this critical gap, LuAG:Ce thin films with Ce concentrations spanning 0.1–4.0 mol% were synthesized via spray pyrolysis. Comparative analysis between low-concentration films, which exhibit low emission and negligible temperature rise, and high-concentration films, marked by intense emission, substantial heating, and evident saturation behavior, enables a systematic deconvolution of optical and thermal contributions. The introduction of active water cooling further isolates the thermal component, confirming its central role in driving saturation under high-power excitation. This approach and these findings inform both compositional and thermal design strategies for the development of next-generation laser-driven phosphor systems optimized for high-power operation.

2 Experimental

2.1 Materials

Lutetium oxide (Lu_2O_3 > 99.99%), aluminum nitrate nonahydrate ($Al(NO_3)_3{\cdot}9H_2O$), and cerium nitrate hexahydrate ($Ce(NO_3)_3{\cdot}6H_2O$), all sourced from Sinopharm Chemical Reagent Co., Ltd., China, were employed as the respective precursors for Lu, Al, and Ce. Lu_2O_3 was first dissolved in nitric acid to yield a lutetium nitrate solution, which was subsequently mixed with stoichiometric amounts of aluminum nitrate and cerium nitrate to form a homogeneous precursor solution with a total cation concentration of 0.1 M. Polyvinylpyrrolidone (PVP; 3 wt%) was added to promote film formation, and the molar ratio of rare earth to aluminum cations was fixed at 3 : 5. Tetraethyl orthosilicate (TEOS, 2 wt%) served as a fluxing agent. The Ce doping concentration was systematically varied from 0.1 to 4.0 mol%. Prior to deposition, sapphire substrates (diameter: 20 mm, thickness: 1 mm; Beijing Xintian Borui Photoelectric Technology Co., Ltd., China) were ultrasonically cleaned in deionized water, acetone, and ethanol.

2.2 Synthesis of LuAG:Ce films

LuAG:Ce thin films were fabricated via spray pyrolysis using a custom-built setup comprising a spray nozzle, peristaltic pump, and programmable *XY*-stage. Substrates were maintained at 800 °C during deposition, with temperature control achieved through a K-type thermocouple. The precursor solution was atomized at a rate of 30 rad·min^{-1} using compressed air (500 kPa) as the carrier gas, with a fixed nozzle-to-substrate distance of 140 mm. Spatial uniformity was ensured by coordinated movement of the nozzle and substrate along orthogonal axes. Each deposition cycle lasted 5 min, followed by annealing at 700 °C for 10 min in a muffle furnace (KSL-1100X, Hefei Kejing Materials Technology Co., Ltd., China). The deposition-annealing cycle was repeated four times to build a multilayer structure. Final crystallization was achieved through postdeposition annealing at 1500 °C for 5 h in a CO atmosphere.

2.3 Characterization techniques

Phase composition was identified via an X-ray diffractometer (XRD; PW 3040/60, PANalytical, the Netherlands) employing Cu Kα radiation (λ = 0.15406 nm) at 40 kV and 200 mA, scanned over a 2θ range of 10°–70° with a step size of 0.02°. Cross-sectional and surface morphologies were examined by a scanning electron microscope (SEM; JSM-7001F, JEOL, Japan) equipped with an energy-dispersive spectrometer (EDS) for elemental analysis. Optical transmittance in the 375–550 nm range was measured using an ultraviolet–visible (UV–Vis) spectrophotometer (Lambda-750S, PerkinElmer, USA) equipped with a 150 mm integrating sphere, while absorption spectra (375–500 nm) were acquired at room temperature using a UV–Vis–near infrared (UV–Vis–NIR) spectrometer (UV-3600i Plus, Shimadzu, Japan). Photoluminescence (PL) and photoluminescence excitation (PLE) spectra were recorded with a steady-state fluorometer (FLS1000, Edinburgh Instruments, UK) equipped with a 150 W pulsed xenon source. Luminous flux, luminous efficiency, blue light absorption, and conversion efficiency were determined using an integrating sphere setup comprising a 450 nm, 30 W blue laser, a 30 cm diameter sphere (Labsphere), and a charge-coupled device (CCD) spectrometer (USB4000, Ocean Optics, USA). The excitation beam was confined to a 0.5 mm^2 area. Emission spectra were analyzed to extract chromaticity coordinates and correlated color temperature (CCT). Internal and external quantum efficiencies were measured using a calibrated, integrating-sphere-based system, with spectral correction procedures applied. Room-temperature thermal conductivity was assessed via the transient plane source method (Hot Disk TPS 2500 S), and mean values were reported. The surface temperature distribution of the samples under laser excitation was recorded using an infrared thermography system (Ti400, Fluke). The system provides a spatial resolution of 0.93 mRad, a thermal sensitivity of better than 0.05 °C, and a standard calibration offering a temperature measurement accuracy of ±2 °C. For tests conducted under water-cooling conditions, the sapphire substrate's backside was coupled to a copper cooling block with thermal grease, using deionized water as a coolant at a flow rate of 500 L·h^{-1}, maintained at 3 °C by an external chiller.

3 Results and discussion

3.1 Structural and morphological characterization of LuAG:Ce thin films

LuAG:Ce thin films were fabricated on sapphire substrates via spray pyrolysis, followed by annealing at 1500 °C for 5 h under a CO reducing atmosphere. XRD analysis confirmed the formation of a phase-pure cubic garnet structure ($Lu_3Al_5O_{12}$, PDF#73-1368), with no detectable secondary phases across a Ce doping range of 0.1–4.0 mol% (Fig. 1(a)). A progressive shift of the (420) diffraction peak from 33.63° to 33.58° was observed with increasing Ce content (Fig. 1(b)), corresponding to a lattice parameter expansion from 11.911 to 11.917 Å (Fig. 1(c)). This shift is consistent with Bragg's law and is attributed to the substitution of larger Ce^{3+} ions (1.143 Å, coordination number (CN) = 8) for smaller Lu^{3+} ions (0.977 Å, CN = 8) at dodecahedral sites [29]. Lattice parameters were obtained through least squares lattice parameter refinement, revealing a linear relationship with Ce concentration in the 0.1–2.5 mol% range (R^2 = 0.98), consistent with Vegard's law and indicating the formation of an ideal solid

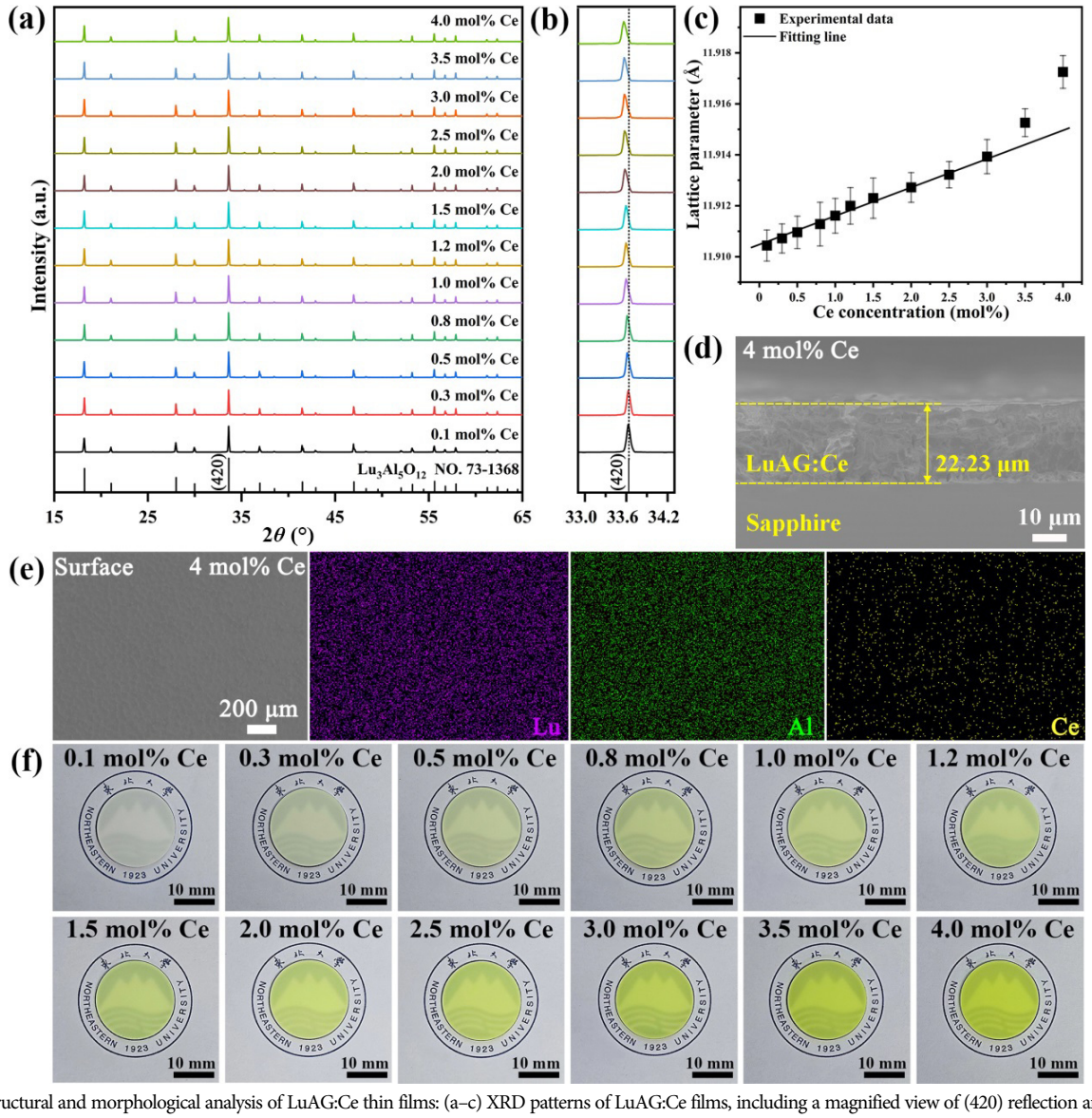

Fig. 1 Structural and morphological analysis of LuAG:Ce thin films: (a–c) XRD patterns of LuAG:Ce films, including a magnified view of (420) reflection and derived lattice parameters, indicating dopant-induced structural variations. (d) Cross-sectional SEM image of a LuAG:Ce film doped with 4 mol% Ce, revealing film thickness and interface quality. (e) Corresponding energy-dispersive EDS elemental map showing spatial distribution of constituent elements and confirming compositional uniformity. (f) Optical photographs of LuAG:Ce films with increasing Ce concentrations, illustrating evolution of film coloration with dopant level.

solution [30]. At concentrations exceeding 2.5 mol%, a deviation from linearity was observed, suggesting the formation of a nonideal solid solution [31]. To quantitatively evaluate the degree of lattice distortion, Williamson–Hall (W–H) analysis [32,33] was conducted to estimate the lattice strain (ε, Table S1 in the Electronic Supplementary Material (ESM)). As shown in Table S1 in the ESM, lattice strain exists in all Ce-doped samples but exhibits a pronounced dependence on Ce concentration. The strain remains nearly constant at low doping levels and then rises sharply once the Ce content exceeds 2.5 mol%. This inflection point coincides with the onset of deviation from Vegard's law. These results demonstrate that excessive Ce incorporation introduces significant lattice distortion, disrupts the ideal solid-solution structure, and consequently deteriorates both luminescence efficiency and thermal stability.

Cross-sectional SEM revealed a uniform film thickness of 22.23 μm with strong interfacial adhesion to the sapphire substrate (Fig. 1(d)), likely arising from interfacial Lu–Al–O chemical bonding [34]. Such robust adhesion is expected to enhance both the thermal and mechanical stability of the films under demanding operating conditions. Notably, films with varying Ce concentrations exhibited similar microstructures, with thicknesses consistently maintained at 22.3±0.5 μm (Fig. S1 in the ESM), underscoring the stability and reproducibility of the synthesis process. EDS elemental mappings (Fig. 1(e)) confirmed the homogeneous distribution of Lu, Al, O, and Ce throughout the films, with no detectable Ce segregation up to 4.0 mol%. A uniform dopant distribution is crucial for preventing the formation of nonradiative recombination centers that would otherwise degrade luminescence performance [35]. Furthermore, EDS point analysis (Fig. S2 and Table S2 in the ESM) verified that the actual Ce contents closely match the nominal concentrations across the entire doping range.

With increasing Ce concentration, the films exhibited a clear macroscopic color transition from pale white–yellow to deep green–yellow (Fig. 1(f)), associated with enhanced absorption in the 400–500 nm spectral range [36]. This absorption band overlaps effectively with the 450 nm emission characteristic of blue LDs, underscoring the films' potential for efficient color conversion in solid-state lighting applications. Importantly,

despite higher doping levels, the films retained optical translucency and remained free from macroscopic defects, maintaining visual clarity over the underlying patterns (Fig. 1(f)).

X-ray photoelectron spectroscopy (XPS) was performed on all films to examine the valence state of the Ce dopant. As reported in Ref. [37], both Ce^{3+} and Ce^{4+} species were present in all samples, even after annealing at 1500 °C in a CO atmosphere (Fig. S3 in the ESM). The concentration of optically active Ce^{3+} ions remained nearly constant across the entire doping range, varying only slightly between 53.3% and 51.1%.

3.2 Spectral evolution and structural implications

The PL characteristics of LuAG:Ce thin films were systematically modulated through controlled variation of Ce doping concentrations. PL excitation spectra, recorded at ~520 nm emission under ambient conditions, revealed distinct Ce^{3+} excitation bands at ~353 and ~450 nm, corresponding to 4f→5d_2 and 4f→5d_1 electronic transitions, respectively (Fig. 2(a)) [38]. Notably, the 450 nm band exhibited markedly higher intensity relative to the 353 nm feature, aligning well with the emission range of commercial blue LDs (445–455 nm), thereby enabling efficient excitation for solid-state lighting applications. Under 450 nm excitation, the emission spectrum displayed a broad band spanning 450–650 nm, originating from 5d_1→4f ($^2F_{5/2}$, $^2F_{7/2}$) transitions (Fig. 2(b)). This yellow–green emission, governed by electric dipole-allowed transitions, reflects strong electron-phonon coupling and is shaped by crystal field effects and local structural interactions [39].

The integrated PL intensity increased with Ce concentration, reaching a maximum at 2.5 mol%, beyond which concentration quenching induced a decline (Fig. 2(c)). At this optimal doping level, the emission intensity was enhanced by a factor of 8.27 compared to the 0.1 mol% sample. Corresponding enhancements in the 4f→5d_2 and 4f→5d_1 excitation bands were observed, with increases of 3.35- and 8.75-fold, respectively. Ultraviolet–visible absorption and transmittance measurements further corroborated these findings (Figs. 2(d) and 2(e)). The absorbance at 450 nm increased monotonically with Ce content, while the transmittance decreased from 45.92% (0.1 mol%) to 24.72% (4.0 mol%), indicating a progressive enhancement in blue-light absorption due to higher dopant content [40]. The absorption observed outside the Ce^{3+} 4f–5d transition bands likely arises from microstructural imperfections such as pores, secondary phases, or grain boundaries [41,42]. Subtle variations in these features can modulate local scattering and absorption behavior, thereby inducing differences in the transmittance.

Quantum efficiency analysis provided additional insight. The internal quantum efficiency (IQE) and external quantum efficiency (EQE) peaked at 89.4% and 62.5%, respectively, at 2.5 mol% Ce under 450 nm excitation, followed by a decline at

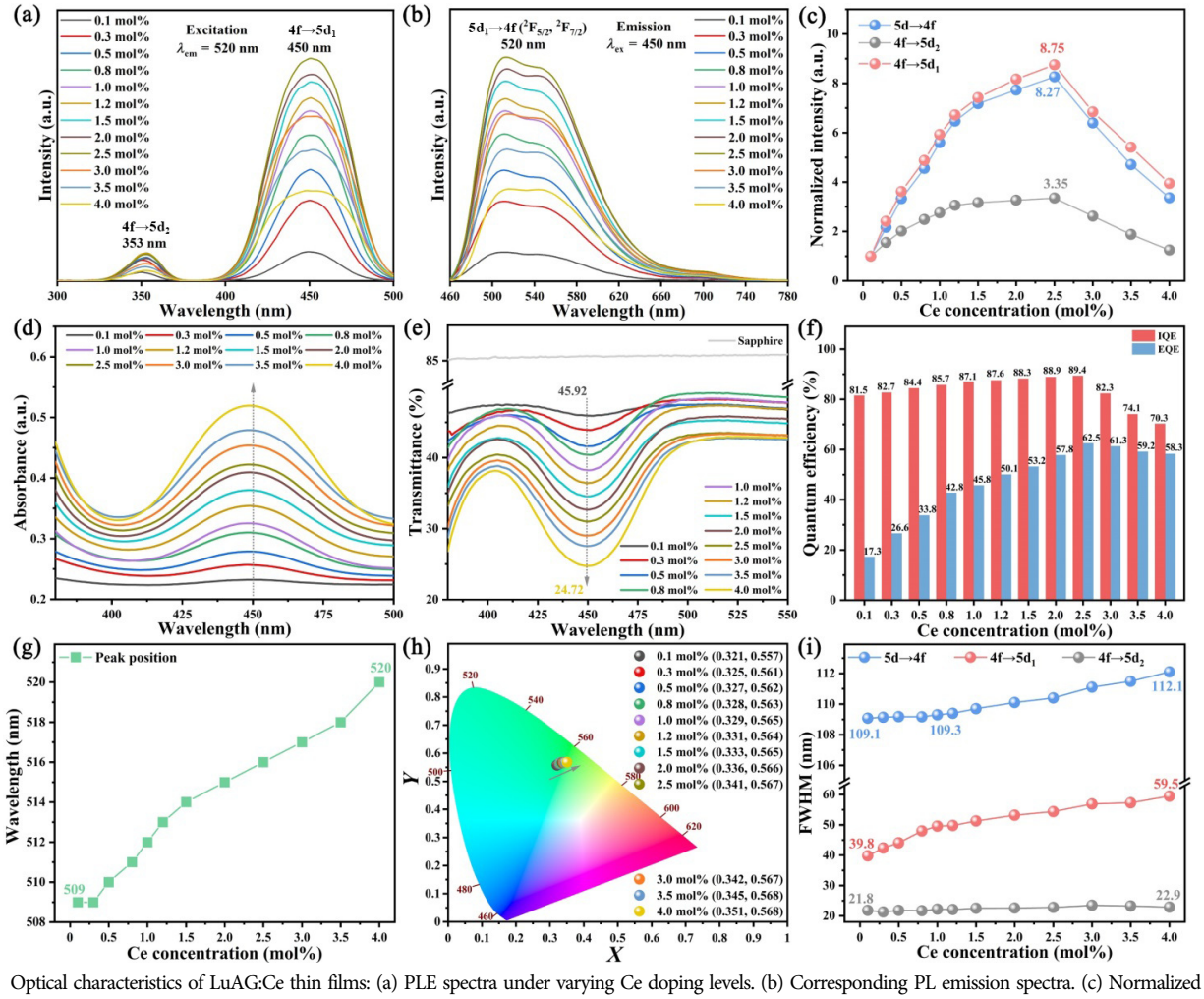

Fig. 2 Optical characteristics of LuAG:Ce thin films: (a) PLE spectra under varying Ce doping levels. (b) Corresponding PL emission spectra. (c) Normalized peak intensities of PLE and PL spectra, highlighting relative changes with doping concentration. (d) Optical absorbance spectra across the examined wavelength range. (e) Transmittance spectra revealing transparency variations among samples. (f) IQE and EQE as a function of Ce content. (g) Evolution of PL emission peak position with increasing dopant concentration. (h) CIE chromaticity coordinates derived from PL emission. (i) FWHM of PL spectra, indicating spectral broadening trends.

higher concentrations. Despite increased absorption, the reduction in PL efficiency at elevated doping levels is attributed to enhanced nonradiative processes [43,44]. Spectral analysis revealed a redshift in the emission peak wavelength from 509 to 520 nm as the Ce concentration increased from 0.1 to 4.0 mol%, accompanied by a shift in the Commission Internationale de l'Éclairage (CIE) coordinates from (0.321, 0.557) to (0.351, 0.568), marking a transition from green to yellow–green emission (Figs. 2(g) and 2(h)). Simultaneously, spectral broadening was evident in the full width at half maximum (FWHM): from 21.8 to 22.9 nm ($4f \rightarrow 5d_2$), from 39.8 to 59.5 nm ($4f \rightarrow 5d_1$), and from 109.1 to 112.1 nm ($5d \rightarrow 4f$) (Fig. 2(i)). These spectral modifications are attributed to increased structural disorder and local environmental heterogeneity at higher doping levels, inducing fluctuations in Ce^{3+} energy levels [45].

3.3 Thermal stability and underlying mechanisms

The development of high-power laser lighting systems necessitates phosphor materials with strong resistance to thermal quenching. PL spectra were recorded under 450 nm excitation across a temperature range of 25–250 °C (Figs. 3(a) and 3(b)). Below 50 °C, all samples maintained over 90% of their room-temperature PL intensity, indicative of minimal thermally induced nonradiative transitions and preserved luminescence efficiency. Beyond this threshold, the PL intensity exhibited a pronounced temperature dependence, with accelerated degradation observed at elevated temperatures, signifying increasing thermally induced nonradiative transitions [46–48].

Thermal stability was strongly influenced by the Ce doping concentration. At 150 °C, the 0.1 mol% Ce sample retained 95.3% of its initial PL intensity, exhibiting remarkable resistance to thermal quenching. In contrast, higher Ce concentrations led to

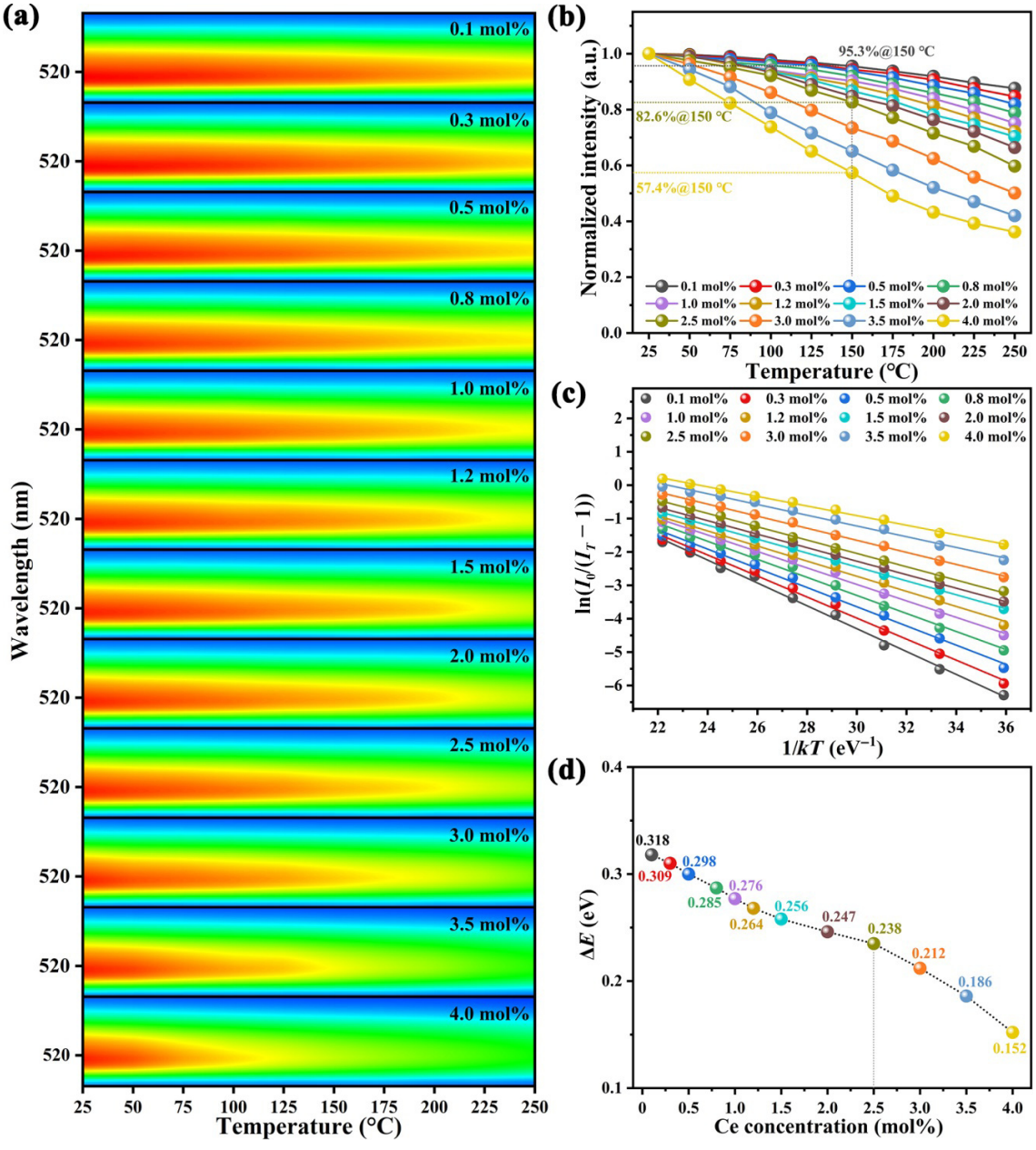

Fig. 3 Temperature-dependent PL of LuAG:Ce films with different Ce concentrations: (a) PL spectra measured between 25 and 250 °C. (b) Normalized PL intensity as a function of temperature, showing thermally induced quenching. (c) Arrhenius plots of $\ln(I_0/I_T - 1)$ vs. $1/kT$ with linear fits. (d) Extracted activation energy (ΔE) for thermal quenching as a function of Ce concentration.

清華大学出版社 Tsinghua University Press | SciOpen

significant quenching: samples with 2.5, 3.0, and 4.0 mol% Ce retained only 82.6%, 65.1%, and 57.4%, respectively. This concentration-dependent quenching is attributed to the increased formation of nonradiative centers and enhanced Ce^{3+}–Ce^{3+} interactions, which promote energy transfer to these centers. XRD further supports this, showing nonideal solid-solution behavior and substantial lattice strain due to excessive Ce-for-Lu substitution, which introduces local distortions that act as nonradiative recombination sites. At elevated temperatures, phonon-assisted energy migration and defect activation exacerbate this quenching behavior [49,50].

To assess the energy barrier for thermal quenching, the ΔE for thermally induced nonradiative transitions was determined using the Arrhenius model [51]:

$$I_T = \frac{I_0}{1 + A\exp(-\Delta E/kT)} \quad (1)$$

where I_0 and I_T denote the PL intensities at 25 °C and temperature T, respectively, A is a preexponential factor, and k is the Boltzmann constant. Linear fitting of the transformed data yielded ΔE values (Figs. 3(c) and 3(d)), which decreased with increasing Ce content, from 0.318 eV at 0.1 mol% to 0.152 eV at 4.0 mol%. This trend suggests that higher dopant concentrations lower the energetic threshold for nonradiative transitions, enabling such pathways to occur at lower temperatures and thereby reducing thermal stability.

A notable transition in ΔE values occurred near 2.5 mol% Ce. Below this concentration, ΔE exhibited a gradual decline, indicating thermally induced nonradiative transitions as the prevailing mechanism. Above 2.5 mol%, ΔE dropped sharply, coinciding with an estimated Ce^{3+}–Ce^{3+} distance below 14.2 Å, an interionic distance that favors Ce^{3+}–Ce^{3+} energy transfer migration [52]. This regime is characterized by energy transfer to nonradiative centers, which accelerates luminescence quenching in samples with 3.0–4.0 mol% Ce [53].

The critical energy transfer distance (R_c) for concentration quenching was calculated to be 17.52 Å (Note S2 in the ESM) [54], which is much larger than the distance required for exchange interactions (< 5 Å) [55]. This strongly suggests that above the critical Ce concentration of 2.5 mol%, long-range multipolar interactions become the dominant mechanism for concentration quenching. This hypothesis was further supported by analyzing the PL intensity as a function of Ce concentration using the log(I/x) vs. log(x) relation (Fig. 4(a)). The obtained exponent θ = 6.34 is consistent with a dipole–dipole interaction mechanism. Consequently, dipole–dipole interactions are identified as the principal quenching pathway for concentrations above 2.5 mol% Ce (Fig. 4(b) and Note S2 in the ESM) [56,57].

3.4 Laser-excited optical properties of uncooled LuAG:Ce thin films

Under 450 nm laser excitation, the optical properties of LuAG:Ce thin films, specifically luminous flux, luminous efficiency (defined as the ratio of luminous flux to incident laser power), blue light absorption, and light conversion efficiency, were systematically investigated across a Ce doping range of 0.1 to 4.0 mol% and excitation power density up to 60 W·mm^{-2} (Figs. 5(a) and 5(d)). These properties demonstrate a strong dependence on both Ce concentration and power density.

At lower Ce concentrations (0.1–0.5 mol%), the luminous flux increased gradually with power density without reaching saturation (Fig. 5(a)). The 0.5 mol% sample achieved a flux of only 1083.9 lm at 60 W·mm^{-2}. This behavior is attributed to the limited density of Ce^{3+} emission centers and low blue light absorption (Fig. 5(c)), which constrains the full utilization of high excitation power despite high light conversion efficiency (Fig. 5(d)) [58].

Conversely, films with higher Ce concentrations (0.8–4.0 mol%) exhibited an initial rapid increase in luminous flux with rising power density, followed by a peak and subsequent decline, indicative of luminous saturation (Fig. 5(a)). For instance, the 2.5 mol% sample reached a maximum of 1618.3 lm at 28 W·mm^{-2} before decreasing. Samples with higher Ce contents (3.0, 3.5, and 4.0 mol%) demonstrated progressively lower saturation thresholds (26, 22, and 16 W·mm^{-2}, respectively) and reduced peak fluxes (1422.7, 1152.5, and 721.9 lm). While increased Ce doping enhances the number of emission centers and improves blue light absorption (Fig. 5(c)), the light conversion efficiency declined with higher Ce concentrations (Fig. 5(d)), reflecting a rise in nonradiative transitions. These results suggest that luminous saturation arises from the competition between radiative and nonradiative transitions.

The luminous efficiency consistently declined with increasing laser excitation power density across all samples (Fig. 5(b)). The 2.5 mol% Ce sample, for example, showed a reduction from 154.1 lm·W^{-1} at 2 W·mm^{-2} to 115.6 lm·W^{-1} at 28 W·mm^{-2}. Similarly, the 4.0 mol% Ce sample experienced a decrease from 120.8 lm·W^{-1} at 2 W·mm^{-2} to 90.2 lm·W^{-1} at 16 W·mm^{-2}. The rate of this decline varied with Ce concentration, exhibiting three distinct regimes: a slow decline (0.1–0.5 mol%), a moderate

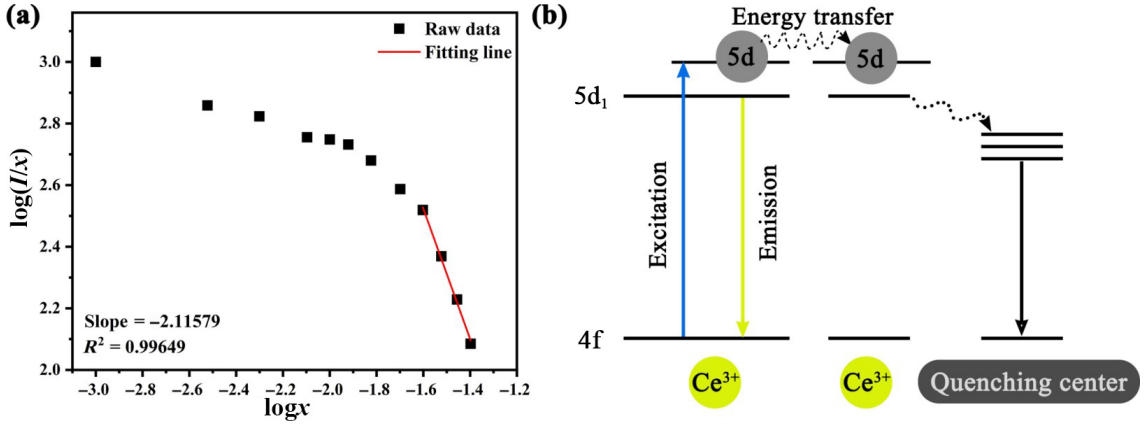

Fig. 4 Concentration quenching in LuAG:Ce thin films: (a) log–log plot of normalized integrated luminescence intensity (log(I/x)) as a function of Ce concentration (log(x)), highlighting occurrence of concentration quenching. (b) Schematic representation of quenching mechanism, depicting energy transfer between adjacent Ce^{3+} ions, followed by nonradiative decay processes.

decline (0.8–2.5 mol%), and a rapid decline (3.0–4.0 mol%). These trends indicate a diminished conversion of input power into luminous flux, primarily due to increasing nonradiative losses. Below 2.5 mol% Ce, thermally activated nonradiative processes are the dominant loss mechanism. Conversely, above 2.5 mol% Ce, concentration-dependent energy transfer, such as dipole–dipole interactions, becomes the predominant factor contributing to efficiency reduction.

Blue light absorption increased with Ce concentration, indicating a greater number of available emission centers for photon capture. At an excitation power density of 2 W·mm^{-2}, the absorption increased from 10.3% at 0.1 mol% Ce to 77.5% at 4.0 mol% Ce (Fig. 5(c)). Across all samples, absorption initially decreased slightly with increasing power density before stabilizing at higher power levels.

Light conversion efficiency, defined as the ratio of emitted yellow light power to absorbed blue light power (Fig. 5(d)), initially increased slightly at low power density but subsequently gradually declined beyond a critical threshold, attributed to increased nonradiative transitions [59]. This conversion efficiency also varied significantly with Ce concentration (Fig. 5(d)). At 15 W·mm^{-2} under 450 nm excitation, the conversion efficiency decreased from 80.4% at 0.1 mol% Ce to 31.4% at 4.0 mol% Ce, primarily driven by escalating nonradiative transitions. Consistent with luminous efficiency trends, thermally activated nonradiative processes are dominant below 2.5 mol% Ce, while concentration-

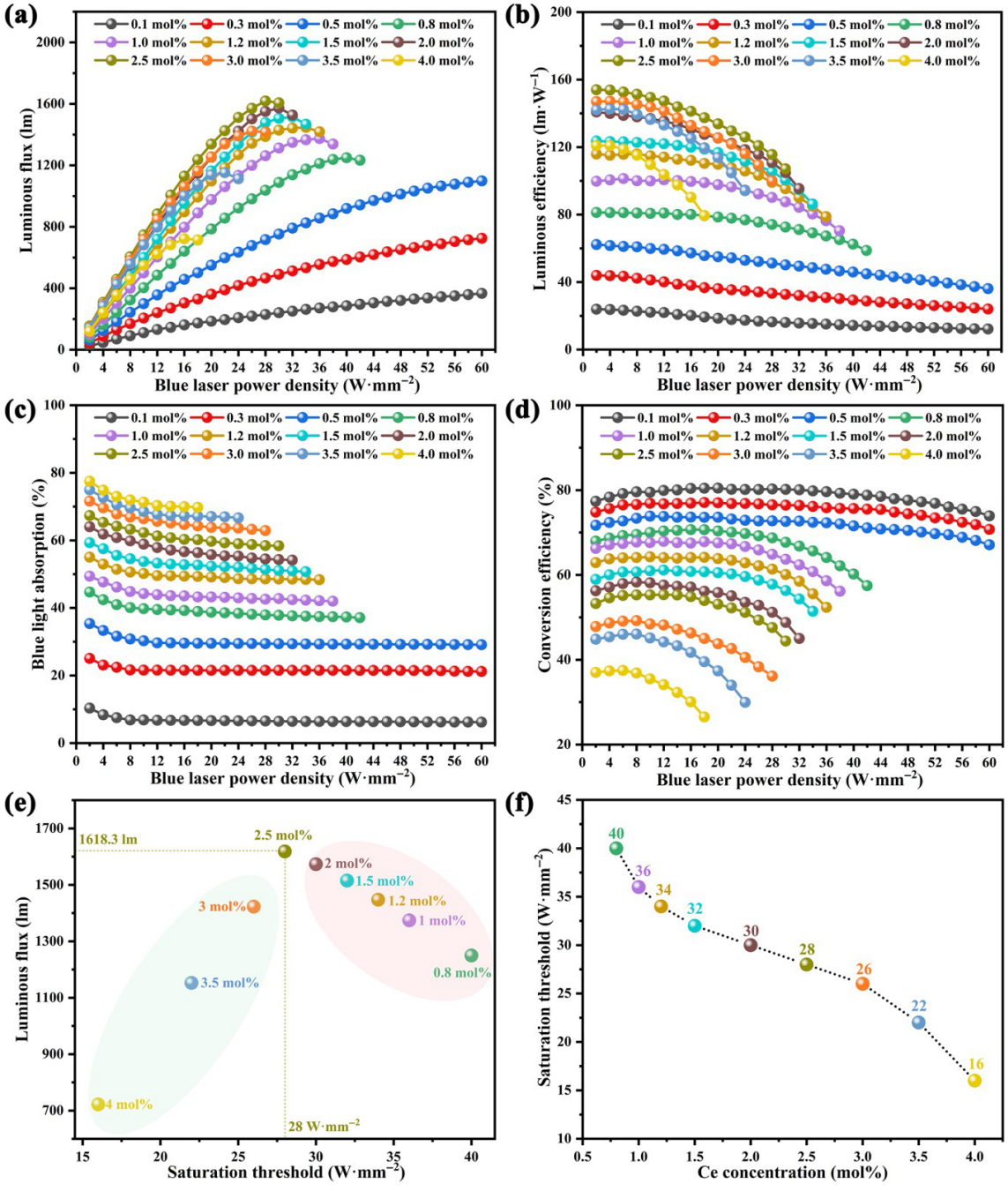

Fig. 5 Laser-excited luminescence characteristics of LuAG:Ce films with varying Ce concentrations: (a) luminous flux, (b) luminous efficiency, (c) blue light absorption, and (d) conversion efficiency as a function of incident blue laser power density. (e) Optimization of luminous flux and saturation threshold for samples with varying Ce concentrations. (f) Decrease in luminous saturation with increasing Ce concentration.

清華大学出版社 Tsinghua University Press | SciOpen

dependent energy transfer (e.g., dipole–dipole interactions) becomes the dominant factor above 2.5 mol% Ce.

The LuAG:Ce thin film with a 2.5 mol% Ce doping concentration exhibited optimal performance (Figs. 5(a), 5(b), and 5(e)) owing to a favorable balance between photon absorption, radiative emission, and nonradiative transitions. Under 450 nm laser excitation at 28 W·mm^{-2}, this composition achieved a luminous flux of 1618.3 lm, with 58.5% blue light absorption and 47.6% light conversion efficiency. Ce concentrations below 0.5 mol% led to diminished luminous output (Fig. 5(a)), primarily due to insufficient absorption and a reduced density of emissive centers. In contrast, concentrations exceeding 2.5 mol% enhanced nonradiative transitions, driven by thermal and concentration quenching, thus compromising luminescent performance (Figs. 5(a), 5(b), and 5(e)). The significant decrease in saturation thresholds, from 40 W·mm^{-2} at 0.8 mol% Ce to 16 W·mm^{-2} at 4.0 mol% Ce (Fig. 5(f)), provides strong evidence of the progressive enhancement of nonradiative processes at higher dopant concentrations, leading to saturation behavior. These findings highlight the critical importance of carefully optimizing the Ce concentration and excitation power density to achieve maximum luminous performance in such materials.

3.5 Heat generation in LuAG:Ce thin films under high-power laser excitation

At low dopant concentrations (0.1–0.5 mol%), the surface temperature rise remains minimal (Figs. 6(a) and 6(b)). For example, the temperature of a 0.1 mol% doped film increases from 19.8 °C at 2 W·mm^{-2} to 45.3 °C at 60 W·mm^{-2}, with similar trends observed for the 0.3 and 0.5 mol% samples. PL and PLE spectra (Fig. 2) reveal a Stokes shift of approximately 0.28 eV,

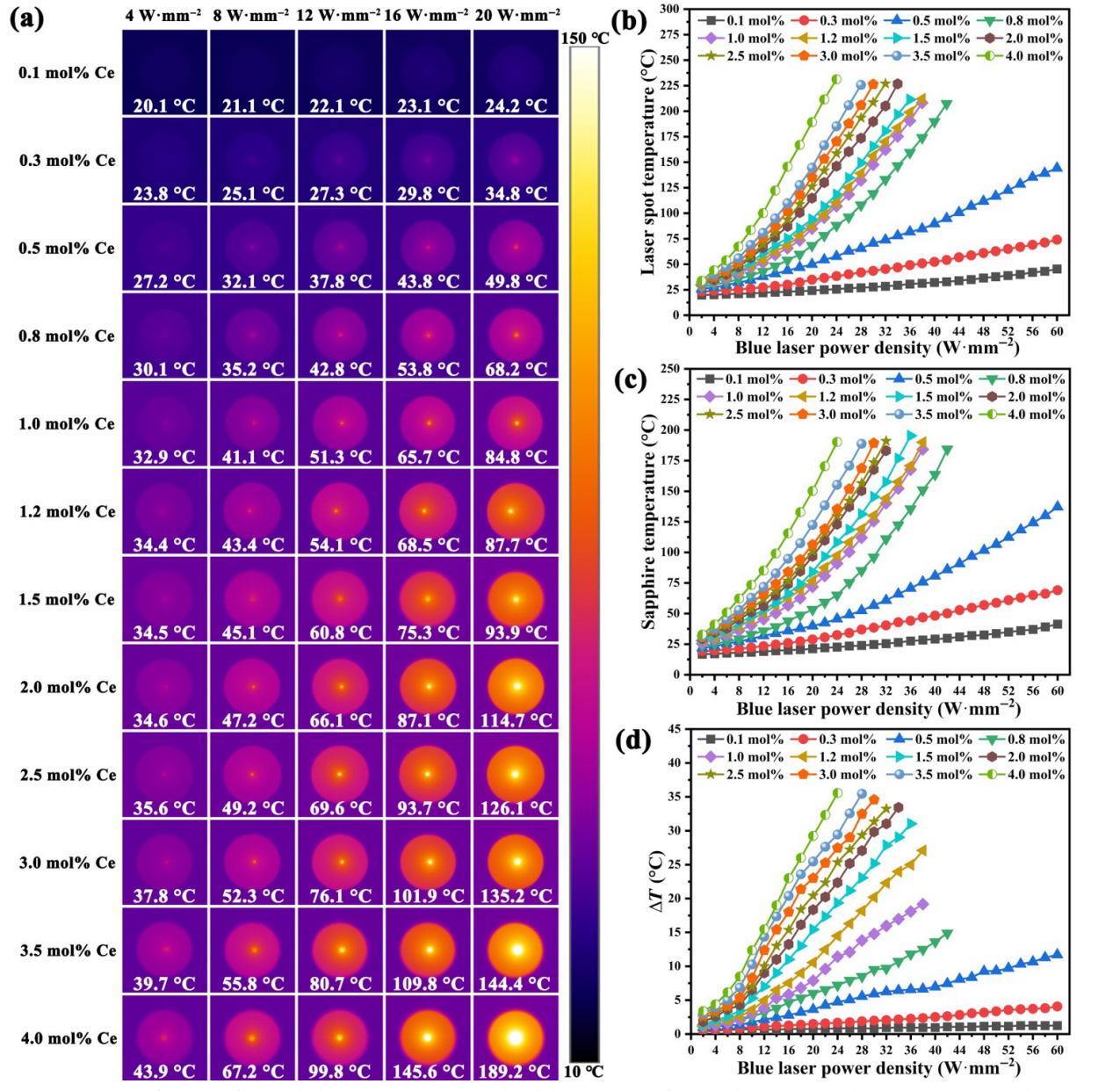

Fig. 6 Thermal behavior of LuAG:Ce films under blue laser excitation: (a) infrared thermal images after 60 s of continuous irradiation at various power densities, with the maximum surface temperature at the excitation spot indicated. (b) Maximum surface temperature at excitation spot as a function of incident power density. (c) Temperature of sapphire substrate directly beneath irradiated region. (d) Temperature difference (ΔT) between maximum surface temperature at excitation spot and underlying sapphire substrate as a function of incident power density.

indicating that nearly 10% of the absorbed photon energy is converted into heat [60–62]. The exceptionally low surface temperatures, even under excitation at 60 W·mm^{-2}, suggest that heat generation is primarily governed by the Stokes shift, with the temperature rise scaling with Ce concentration. Consequently, lower Ce concentrations result in reduced heat generation, leading to significantly lower surface temperatures under intense laser irradiation.

In contrast, intermediate doping levels (0.8–2.5 mol%) show a steeper temperature rise (Figs. 6(a) and 6(b)), reflecting enhanced heat generation from the Stokes shift. At higher concentrations (3.0–4.0 mol%), the rise accelerates sharply, driven not only by Stokes shift-related energy loss but also by concentration quenching, where Ce^{3+}–Ce^{3+} dipole–dipole interactions dissipate additional energy as heat. The combined action of these processes produces extreme heating in heavily doped films, accompanied by diminished luminescence efficiency and reduced saturation thresholds, as evidenced by the lower threshold at 4.0 mol% (16 W·mm^{-2}) relative to 2.5 mol% (28 W·mm^{-2}). Collectively, these results highlight a key trade-off: low Ce concentrations favor efficient light conversion, higher luminous saturation, and minimal heating, whereas high concentrations inevitably induce excessive heat generation, reduced efficiency, and lower saturation thresholds.

Efficient thermal management is essential for the stable operation of high-power laser illumination systems. LuAG:Ce thin films deposited on sapphire substrates exhibit favorable thermal transport characteristics (Figs. 6(c) and 6(d)), owing to the inherently high thermal conductivity of sapphire (~18.11 W·m^{-1}·K^{-1} at room temperature). The thermal conductivity of the LuAG:Ce layer is modulated by the Ce concentration, resulting in a composite conductivity that decreases

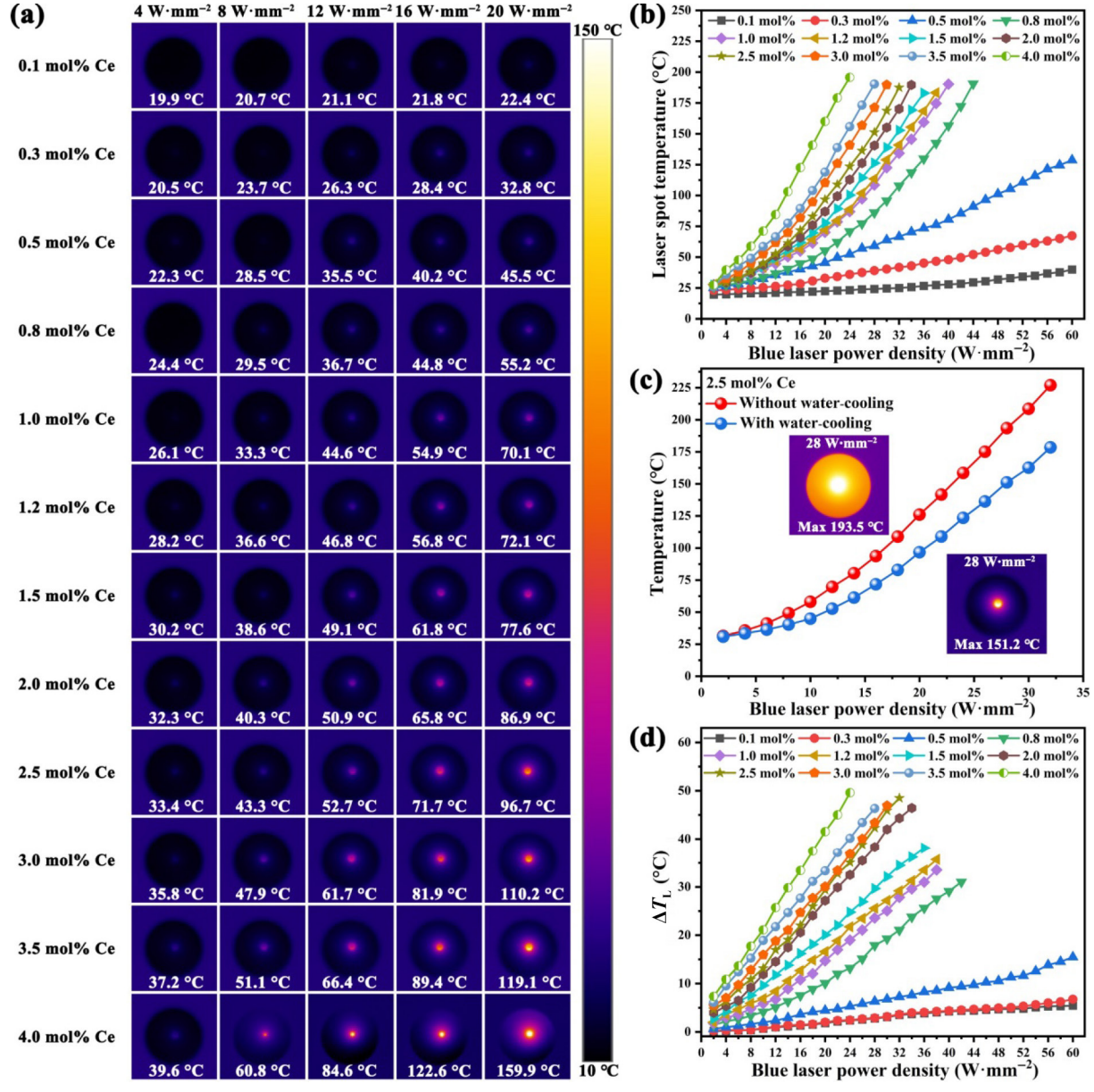

Fig. 7 Mitigation of thermal accumulation in laser-excited LuAG:Ce thin films via water cooling: (a) Infrared thermal images after 60 s of continuous blue laser irradiation at different power densities under active cooling, with the maximum surface temperature at excitation spot indicated. (b) Maximum surface temperature at excitation spot as a function of incident power density, showing thermal response under cooling. (c) Maximum surface temperature of LuAG:Ce films doped with 2.5 mol% Ce vs. excitation power density, demonstrating suppression of thermal buildup by cooling. (d) ΔT_L, the temperature without water cooling minus the temperature with water cooling), plotted against power density for films with varying Ce concentrations.

from 14.97 W·m^{-1}·K^{-1} at 0.1 mol% to 12.08 W·m^{-1}·K^{-1} at 4.0 mol% Ce (Fig. S4 in the ESM). Temperature measurements under laser excitation confirm effective heat transfer across the film-substrate interface, as indicated by minimal thermal gradients (ΔT) between the irradiated film surface and the underlying sapphire substrate (Figs. 6(c) and 6(d)). Under 20 W·mm^{-2} excitation, the 2.5 mol% Ce-doped film reached a surface temperature of 126.1 °C, while the corresponding substrate temperature was 101.1 °C. For the 4.0 mol% sample, temperatures of 189.2 °C (film) and 150.2 °C (substrate) were recorded. These relatively low temperature differentials highlight the role of the substrate in dissipating heat and underscore the suitability of LuAG:Ce/sapphire heterostructures for high-power laser-based applications.

3.6 Water cooling for temperature suppression and enhanced luminous performance

Under intense laser excitation, LuAG:Ce thin films experience a temperature rise, with the magnitude of the increase depending on the Ce concentration. This rise is primarily driven by heat generated from the Stokes shift. The elevated temperature enhances nonradiative transitions, which compete with radiative emission, thereby reducing PL efficiency. Effective thermal management is crucial to control this rise and maintain optical performance. To this end, a water-cooling system was implemented to mitigate the temperature increase.

Water cooling effectively reduced local temperatures, with the extent of temperature reduction (ΔT_L) strongly depending on the doping level and excitation power density (Figs. 7(a)–7(d)). Films doped with 0.1–0.3 mol% Ce exhibited minimal heat generation and correspondingly small ΔT_L values. In contrast, films with higher dopant concentrations (0.5–4.0 mol%) generated substantial heat under uncooled conditions, leading to significant temperature reductions with active cooling. For instance, a 2.5 mol% Ce-doped sample exhibited temperature reductions of 13.2, 29.4, and 42.3 °C at excitation power densities of 10, 20, and 28 W·mm^{-2}, respectively (Fig. 7(c)). These results demonstrate that water cooling becomes increasingly effective at higher excitation power densities and dopant concentrations, where heat generation and thermal accumulation are most severe.

Luminous performance was significantly influenced by water cooling (Figs. 8, 9, and S5 in the ESM). At low doping concentrations (0.1–0.5 mol%), water cooling resulted in

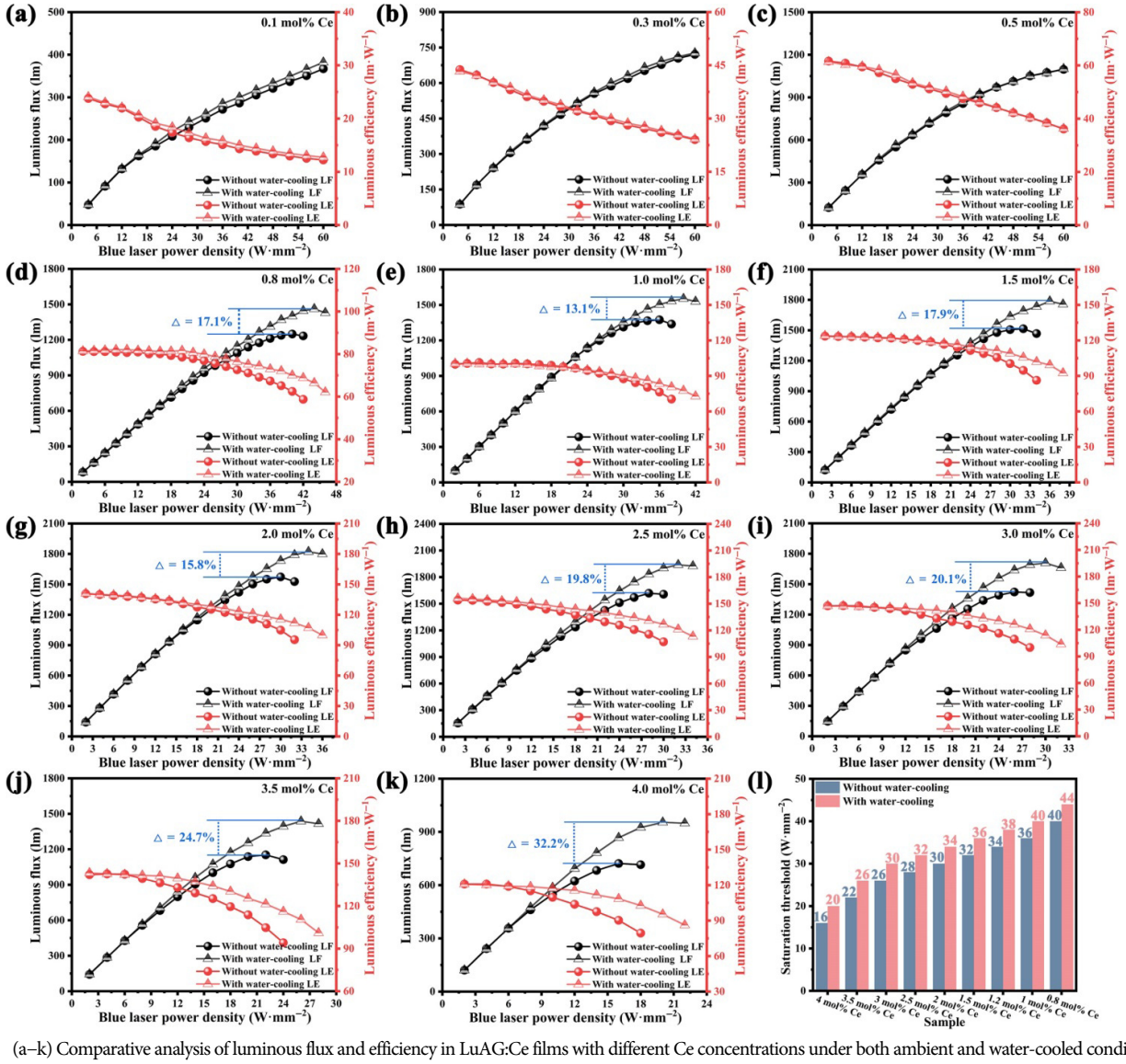

Fig. 8 (a–k) Comparative analysis of luminous flux and efficiency in LuAG:Ce films with different Ce concentrations under both ambient and water-cooled conditions. (l) Water cooling significantly enhances saturation threshold across entire range of Ce concentrations, highlighting critical role of temperature reduction in optimizing performance of high-power laser-excited luminescence.

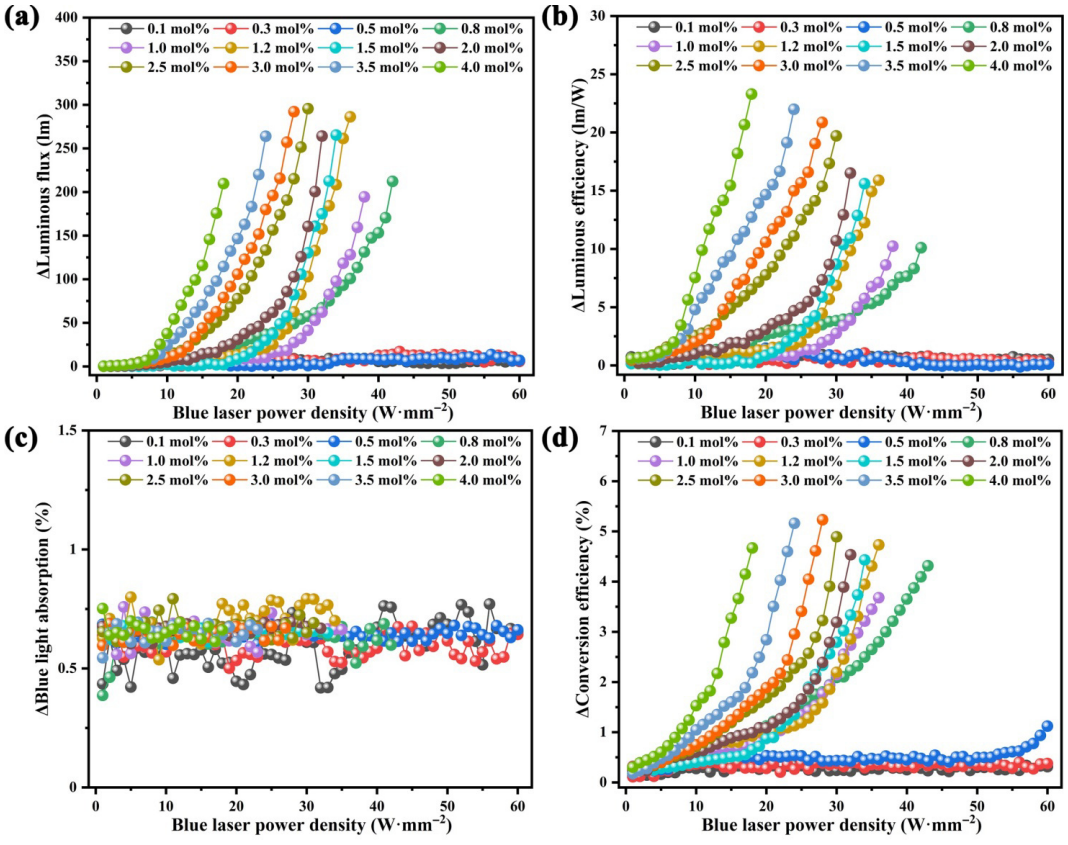

Fig. 9 Differences in (a) luminous flux, (b) luminous efficiency, (c) blue light absorption, and (d) conversion efficiency of LuAG:Ce films, calculated as values under water cooling minus those under ambient conditions, highlighting effect of water cooling on these characteristics.

negligible improvements, with increases in luminous flux and efficiency remaining below 4% (Figs. 8(a)–8(c), 9(a), and 9(b)). For example, a 0.1 mol% sample under 60 W·mm^{-2} excitation showed only a slight enhancement in luminous flux (from 366.9 to 382.2 lm) and efficiency (from 12.2 to 12.7 lm·W^{-1}). These results suggest minimal thermal quenching in this regime. In contrast, films with intermediate doping levels (0.8–2.5 mol%) exhibited greater thermal sensitivity, with water cooling leading to substantial increases in the saturation threshold, luminous flux, and efficiency (Figs. 8(d)–8(h) and 9(a) and 9(b)). A 0.8 mol% sample showed a shift in saturation threshold from 40 to 44 W·mm^{-2}, accompanied by 17.1% and 6.4% increases in luminous flux and efficiency, respectively. Optimal performance was observed at 2.5 mol% Ce, where water cooling raised the saturation threshold from 28 to 32 W·mm^{-2}, luminous flux from 1618.3 to 1938.6 lm (a 19.8% increase), and efficiency from 115.6 to 121.2 lm·W^{-1} (a 4.8% increase). These improvements are attributed to the reduction in temperature, which suppressed thermally activated nonradiative transitions.

At higher doping levels (3.0–4.0 mol%), heat generation, driven by concentration quenching and the Stokes shift, becomes significantly more pronounced. The application of water cooling effectively reduces the temperature, thereby mitigating thermal quenching effects (Figs. 8(i)–8(k), 9(a), and 9(b)). For example, a sample with 3.5 mol% Ce exhibited an 18.2% increase in the saturation threshold (from 22 to 26 W·mm^{-2}), a 24.7% enhancement in luminous flux (from 1152.5 to 1437.2 lm), and a 5.5% improvement in luminous efficiency (from 104.8 to 110.6 lm·W^{-1}). Despite these improvements, the luminous output within this concentration range remained constrained by nonradiative transitions, primarily due to both concentration and thermal quenching effects.

Water cooling significantly elevates the saturation threshold across all Ce concentrations examined (Fig. 8(l)), highlighting the critical role of temperature reduction in optimizing high-power laser-excited luminescence performance. Notably, a sustained decrease in the saturation threshold is observed with increasing Ce concentration, even under water-cooling conditions (Fig. 8(l)). These findings emphasize the complex interaction between radiative emission and nonradiative transitions, ultimately leading to luminous saturation.

The absorption of incident blue light remained nearly unchanged (Δ blue light absorption < 1%) across all Ce concentrations when comparing values obtained under water-cooled and ambient conditions (Fig. 9(c)), indicating that temperature reduction has a negligible effect on intrinsic optical absorption. The light conversion efficiency showed minimal improvement at low doping levels (0.1–0.5 mol%) but exhibited a significant enhancement in the 0.8–4.0 mol% range, driven by a remarkable temperature reduction that mitigated thermally induced nonradiative transitions (Fig. 9(d)). These observations underscore the dominant role of heat generation, induced by the Stokes shift, as the primary factor limiting luminous performance.

High-power operational stability (without water cooling) was assessed for the 2.5 mol% sample under continuous 25 W·mm^{-2} excitation. The emission spectra retained stable yellow–green profiles (460–650 nm) with a residual 450 nm laser peak (Fig. 10(a)). The luminous flux declined to 86.4% after 30 s and stabilized at 83.5% after 1800 s (Fig. 10(b)). Blue light absorption exhibited a modest drop from 97.8% to 97.2% (Fig. 10(c)), while the conversion efficiency decreased from 100% to 88.2% over 30 s, stabilizing at 84.7% thereafter, indicative of favorable thermal robustness (Fig. 10(d)).

The chromaticity coordinates (CIE of 0.29 and 0.49) remained

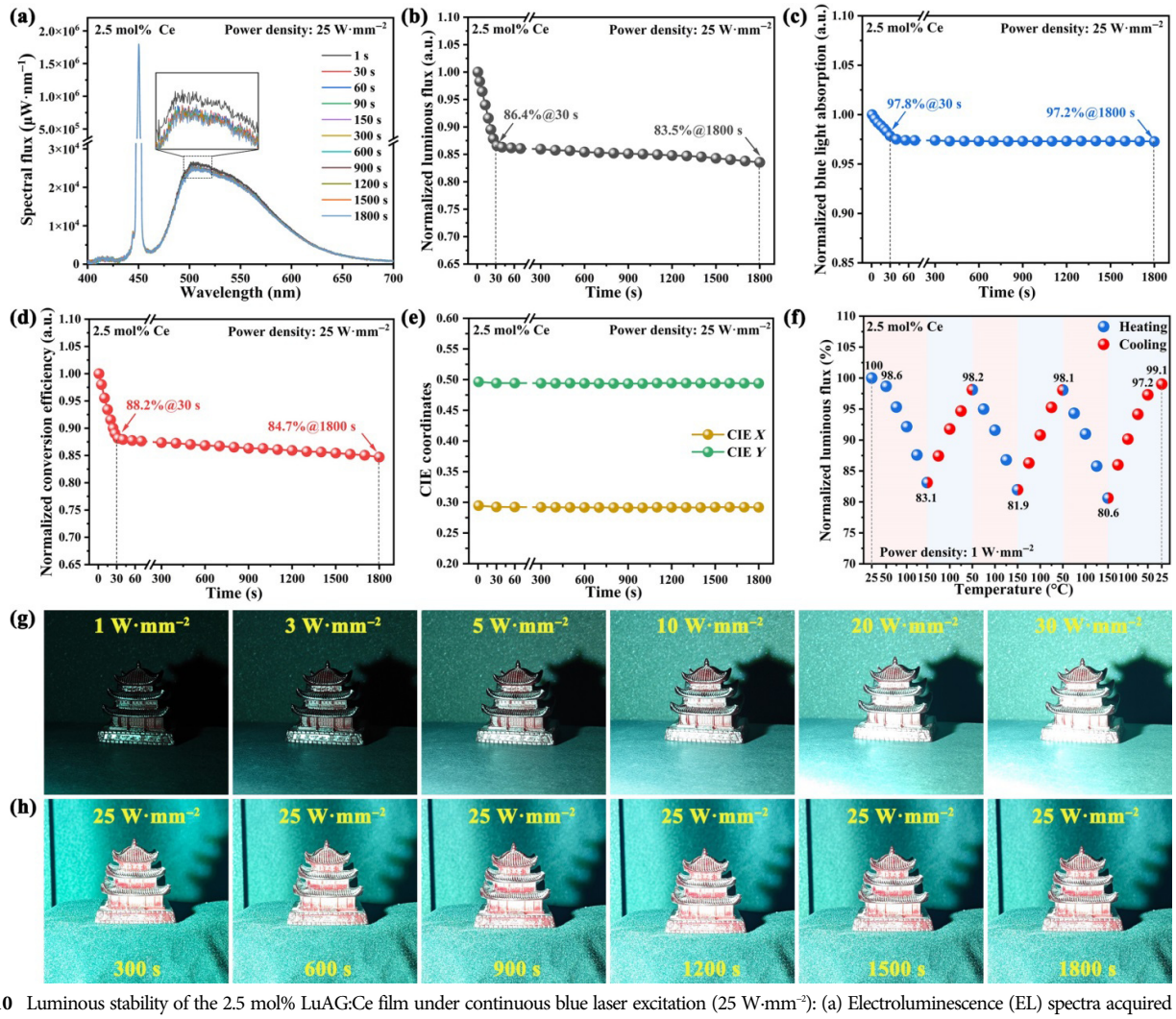

Fig. 10 Luminous stability of the 2.5 mol% LuAG:Ce film under continuous blue laser excitation (25 W·mm^{-2}): (a) Electroluminescence (EL) spectra acquired under sustained blue laser irradiation, illustrating spectral evolution as a function of exposure time. (b) Normalized luminous flux as a function of time under constant excitation. (c) Temporal changes in normalized blue light absorption under sustained excitation. (d) Evolution of normalized conversion efficiency during extended excitation. (e) Time-dependent CIE chromaticity coordinates. (f) Relative luminous flux recorded across three thermal cycles (25–150 °C) at a constant excitation power density of 1 W·mm^{-2}. (g) Emission behavior of film under varying excitation power densities. (h) Luminescence characteristics at a fixed power density of 25 W·mm^{-2} at different excitation durations.

invariant under extended excitation, confirming minimal spectral distortion (Fig. 10(e)). Thermal cycling between 25 and 150 °C (25 °C·min^{-1} ramp, three cycles, 1 W·mm^{-2} excitation) revealed nonlinear but reversible luminous variation (Fig. 10(f)). The flux dropped by 16.9% at 150 °C during the first cycle and recovered to 98.2% at 50 °C. Subsequent cycles yielded repeatable behavior with a cumulative loss below 0.9%, indicating strong thermal resilience. The illumination intensity increased significantly with excitation power (1–30 W·mm^{-2}) and remained stable over prolonged operation (Figs. 10(g) and 10(h)), highlighting the suitability of Ce-doped LuAG thin films, particularly at 2.5 mol%, for high-power laser lighting applications.

4 Conclusions

The opto-thermal characteristics of LuAG:Ce thin films fabricated using spray pyrolysis are primarily influenced by both Ce concentration and excitation power density. The following key insights have been established:

1) Heat generated from the Stokes shift causes an increase in temperature, which is dependent on both Ce concentration and excitation power density. Elevated temperatures promote nonradiative transitions (thermal quenching). The implementation of water cooling effectively mitigates thermal quenching, raising saturation thresholds and improving luminous performance. Specifically, the 2.5 mol% Ce composition achieved a luminous flux of 1938.6 lm under 32 W·mm^{-2} excitation. This composition also demonstrated excellent spectral stability and high luminous retention during prolonged high-power operation, highlighting its practical applicability.

2) Nonradiative transitions, arising from thermal quenching, lead to luminous saturation. The saturation threshold exhibits a strong dependence on the Ce concentration, with a systematic reduction observed as the Ce concentration increases.

3) This study conclusively demonstrates the dominant role of heat generation in limiting the performance of laser-driven lighting systems. The insights gained provide a clear framework for design, focusing on Ce dopant concentration and heat dissipation strategies. This work lays the groundwork for future research aimed at inhibiting heat generation and developing efficient heat dissipation architectures, both of which are essential for achieving improved performance in high-power solid-state lighting applications.

Acknowledgements

This work was supported by the National Natural Science Foundation of China (Nos. 51977027 and 51967008), the Natural Science Foundation of Liaoning Province (No. 2025-MS-038), and the Scientific and Technological Project of Yunnan Precious Metals Laboratory (Nos. YPML-2023050250, YPML-2022050206, YPML-20240502061, YPML-20240502062, and YPML-20240502091).

Availability of data and materials

The data that support the findings of this study are available from the corresponding author upon reasonable request.

Competing interests

The authors have no competing interests to declare that are relevant to the content of this article.

Electronic Supplementary Material

Supplementary material is available in the online version of this article at https://doi.org/10.26599/JAC.2026.9221238.

References

[1] Yang CC, Zhang XY, Kang J, *et al.* Recent progress on garnet phosphor ceramics for high power solid-state lighting. *J Mater Sci Technol* 2023, **166**: 1–20.

[2] Wang TT, Xue BG, Cui H, *et al.* Ultrasonic spray pyrolysis synthesis and photoluminescence of LuAG:Ce thin films. *Materials* 2022, **15**: 2577.

[3] Li SX, Huang LH, Guo YQ, *et al.* A super-high brightness and excellent colour quality laser-driven white light source enables miniaturized endoscopy. *Mater Horiz* 2023, **10**: 4581–4588.

[4] Guo YQ, Wang GJ, Qiu LR, *et al.* Achieving ultra-brightness green light source with electro-optical conversion efficiency up to 26.3% for underwater wireless optical communication. *Adv Funct Mater* 2025, **35**: 2506929.

[5] Cheng ZQ, Liu X, Chen XR, *et al.* Composition and luminescence properties of highly robust green-emitting LuAG:Ce/Al_2O_3 composite phosphor ceramics for high-power solid-state lighting. *J Adv Ceram* 2023, **12**: 625–633.

[6] Zhu YW, Li Y, Wang TT, *et al.* Optical path coupling regulation of excitation light and LuAG:Ce phosphor ceramics for high-luminous-efficiency laser lighting. *J Lumin* 2025, **283**: 121256.

[7] Ma YL, Li XC, Wu L, *et al.* Efficient thermal and luminescent regulations of LuAG:Ce-PiG based remote LED/LD. *Ceram Int* 2024, **50**: 4831–4840.

[8] Hu HY, Xue BG, Liu SH, *et al.* Lowering operating temperatures in high-power laser-excited LuAG:Ce films by improving crystallinity and increasing Ce^{3+} content. *J Adv Ceram* 2025, **14**: 9221061.

[9] Liu SH, Xue BG, Zhou LM, *et al.* Tailoring thermal behavior and luminous performance in LuAG:Ce films via thickness control for high-power laser lighting applications. *Rare Met* 2024, **43**: 6537–6548.

[10] Liu X, Chen MX, Zhao JZ, *et al.* Unique composite architecture of phosphor-in-glass film coated on different heat-conducting substrates for high-brightness laser lighting. *J Adv Ceram* 2025, **14**: 9221027.

[11] Wang YB, Cheng ZQ, Zhou ZZ, *et al.* Pore-coexisting $BaAl_2O_4$–LuAG:Ce composite phosphor ceramics for solid-state lighting. *J Adv Ceram* 2025, **14**: 9221156.

[12] Ma YH, Gao X, Zhang WT, *et al.* Enhanced red luminescence of $Ca_3Si_{2-x}M_xO_7$:Eu^{3+} (M = Al, P) phosphors via partial substitution of Si^{4+} for applications in white light-emitting diodes. *Rare Met* 2024, **43**: 736–748.

[13] Tian RD, Wang QH, Li SX, *et al.* Efficient $Sr_{0.5}Ca_{0.5}AlSiN_3$:Eu^{2+} red-emitting ceramics for high-power solid-state lighting. *J Mater Sci Technol* 2025, **210**: 179–187.

[14] Cheng H, Wang Y, Peng JA, *et al.* Novel alumina heat sink structure for enhanced thermal management of phosphor-in-glass film enabling high saturation threshold in high-brightness laser lighting. *Opt Laser Technol* 2026, **193**: 114230.

[15] Bachmann V, Ronda C, Meijerink A. Temperature quenching of yellow Ce^{3+} luminescence in YAG:Ce. *Chem Mater* 2009, **21**: 2077–2084.

[16] Yang ZY, de Boer T, Braun PM, *et al.* Thermally stable red-emitting oxide ceramics for laser lighting. *Adv Mater* 2023, **35**: 2301837.

[17] Sun YS, Wang YZ, Chen WB, *et al.* Rapid synthesis of phosphor-glass composites in seconds based on particle self-stabilization. *Nat Commun* 2024, **15**: 1033.

[18] Li SX, Tian RD, Yan TY, *et al.* Small-sized nitride phosphors achieving mini-LED backlights with superhigh brightness and ultralong durability. *Mater Today* 2023, **70**: 82–92.

[19] Zheng P, Li SX, Takeda T, *et al.* Unraveling the luminescence quenching of phosphors under high-power-density excitation. *Acta Mater* 2021, **209**: 116813.

[20] Lin SS, Lin H, Wang PF, *et al.* An orange–yellow-emitting $Lu_{2-x}Mg_2Al_{2-y}Ga_ySi_2O_{12}$:$xCe^{3+}$ phosphor-in-glass film for laser-driven white light. *J Mater Chem C* 2023, **11**: 1530–1540.

[21] Liao SX, Jin SL, Pang T, *et al.* Novel color converters for high brightness laser-driven projection display: Transparent ceramics–glass ceramics film composite. *Adv Funct Mater* 2024, **34**: 2307761.

[22] Kang J, Zhang L, Li YB, *et al.* Luminescence declining behaviors in YAG:Ce transparent ceramics for high power laser lighting. *J Mater Chem C* 2019, **7**: 14357–14365.

[23] Liu BG, Guo YH, Li YZ, *et al.* Enhanced luminous exitance and saturation threshold of $Y_3Al_5O_{12}$:Ce phosphor-in-glass films via incorporation of highly thermally conductive boron nitride particles. *Opt Mater* 2025, **163**: 116973.

[24] Xu YR, Li SX, Zheng P, *et al.* A search for extra-high brightness laser-driven color converters by investigating thermally-induced luminance saturation. *J Mater Chem C* 2019, **7**: 11449–11456.

[25] Zhang YQ, Liu JM, Zhang YJ, *et al.* Robust YAG:Ce single crystal for ultra-high efficiency laser lighting. *J Rare Earth* 2022, **40**: 717–724.

[26] Wang YB, Cheng ZQ, Ye JH, *et al.* Ce:LuAG transparent ceramics for high-brightness solid-state lighting: Fabrication and effect of Ce concentration. *Opt Mater* 2024, **147**: 114697.

[27] Yu ZK, Li JY, Zhao JZ, *et al.* High luminescence saturation $Y_3Al_5O_{12}$:Ce^{3+}-diamond composite color converter for high-brightness laser-driven white lighting. *Laser Photonics Rev* 2025, **19**: 2401124.

[28] Zhang HJ, Zhao JZ, Yu ZK, *et al.* A novel sapphire@PiGF@sapphire color converter with high luminescence saturation threshold for laser lighting. *Adv Funct Mater* 2025, **35**: 2414023.

[29] Xu J, Fan LC, Shi Y, *et al.* Effects of Ce^{3+} doping concentrations on microstructure and luminescent properties of Ce^{3+}:$Lu_3Al_5O_{12}$ (Ce:LuAG) transparent ceramics. *Opt Mater* 2014, **36**: 1954–1958.

[30] Tobeck C, Wende H, Ruschewitz U. Solid solutions $Ln_xU_{1-x}C_2$ with Ln = Tb, Dy, Ho, Tm, and Lu showing ideal vegard behavior. *Inorganics* 2023, **11**: 457.

[31] Krutyak N, Nagirnyi V, Zadneprovski B, *et al.* Influence of composition on luminescence properties of $Cd_{1-x}Zn_xWO_4$ solid solutions. *J Lumin* 2024, **267**: 120356.

[32] Choudhury T, Kumi-Barimah E, Parameswaran Nampi P, *et al.* Influence of lattice strain on Er^{3+} ions activated magnesium zirconium phosphate phosphors: Morphological, structural, and photoluminescence properties. *Mater Sci Eng B-Adv* 2022, **277**: 115582.

[33] Poria K, Bhatia S, Kashyap R, *et al.* Structural and luminescence properties of novel Eu^{3+}-doped $Na_3Ba_2LaNb_{10}O_{30}$ phosphors with high quantum efficiency and excellent color purity for w-LED applications. *RSC Adv* 2024, **14**: 29490–29504.

[34] Abe Y, Yi E, Laine RM. Processing thin, dense, transparent Ce:$Y_3Al_5O_{12}$ films from flame made nanopowders for white light applications. *J Eur Ceram Soc* 2019, **39**: 4972–4978.

[35] Sang PF, Zhang L, Kang J, *et al.* Composite structure Al_2O_3/Al_2O_3–YAG:Ce/YAG ceramics with high color spatial uniformity for white laser lighting. *J Adv Ceram* 2024, **13**: 189–197.
[36] Ling JR, Xu WT, Yang J, *et al.* The effect of Lu^{3+} doping upon YAG:Ce phosphor ceramics for high-power white LEDs. *J Eur Ceram Soc* 2021, **41**: 5967–5976.
[37] Yao Q, Hu P, Sun P, *et al.* YAG:Ce^{3+} transparent ceramic phosphors brighten the next-generation laser-driven lighting. *Adv Mater* 2020, **32**: 1907888.
[38] Zhang PY, Zhang YF, Xue BG, *et al.* YAG:Ce films for laser-driven white lighting: Annealing temperature and atmosphere-controlled luminescence performances. *J Alloys Compd* 2024, **972**: 172826.
[39] Tian YN, Chen J, Yi XZ, *et al.* Unravel the effect of lattice distortion on the 4f–5d excitation of Ce^{3+} in garnet phosphors. *J Alloys Compd* 2022, **907**: 164412.
[40] Yi XZ, Sai QL, Tian YN, *et al.* Fluorescence output enhancement of Ce^{3+}:YAG transparent ceramics by eutectic soldering packaging. *Materials* 2025, **18**: 1081.
[41] Zhang Y, Ling JR, Li YN, *et al.* Blue-green emitting LuASG:Ce phosphor ceramics with high luminous efficacy for high-power LEDs. *J Lumin* 2022, **247**: 118886.
[42] Hu S, Lu CH, Zhou GH, *et al.* Transparent YAG:Ce ceramics for WLEDs with high CRI:Ce^{3+} concentration and sample thickness effects. *Ceram Int* 2016, **42**: 6935–6941.
[43] Qian D, Jin YH, Li ZZ, *et al.* Constructing broadband near-infrared garnet emitters $CaGd_2Ga_4SiO_{12}$:Cr^{3+} with unity quantum efficiency and high thermal stability for versatile applications. *Small* 2025, **21**: 2411804.
[44] Zhang XD, Liu YF, Hu P, *et al.* Hydrolytic-resistance long-persistent luminescence $SrAl_2O_4$:Eu^{2+}, Dy^{3+} ceramics for optical information storage. *Adv Funct Mater* 2025, **35**: 2414872.
[45] Xia ZG, Meijerink A. Ce^{3+}-doped garnet phosphors: Composition modification, luminescence properties and applications. *Chem Soc Rev* 2017, **46**: 275–299.
[46] Lin YC, Erhart P, Karlsson M. Vibrationally induced color shift tuning of photoluminescence in Ce^{3+}-doped garnet phosphors. *J Mater Chem C* 2019, **7**: 12926–12934.
[47] Chen S, Lu ZW, Liu YF, *et al.* Enhanced thermally stability and broadened emission for $Gd_3Ga_5O_{12}$:Cr^{3+} phosphors via Si_3N_4 substitution. *Laser Photonics Rev* 2025, **19**: 2401163.
[48] Liu ZH, Hu P, Feng DK, *et al.* Laminated composite of ceramic/glass films to realize high luminous efficiency and high color quality in laser-driven white lighting. *J Mater Chem C* 2024, **12**: 11898–11906.
[49] George NC, Pell AJ, Dantelle G, *et al.* Local environments of dilute activator ions in the solid-state lighting phosphor $Y_{3-x}Ce_xAl_5O_{12}$. *Chem Mater* 2013, **25**(20): 3979–3995.
[50] Hu P, Liu YF, Sun P, *et al.* Ba^{2+}-Si^{4+}-incorporated high-efficiency and excellent thermal stable YAG:Ce^{3+} ceramic phosphors for laser-driven lighting. *Adv Opt Mater* 2024, **12**: 2401672.
[51] Ma YL, Li XC, Wu L, *et al.* Preparation of $(Lu, Y)_3(Al, Sc, Cr)_2Al_3O_{12}$ phosphor ceramics with high thermal stability for near-infrared LED /LD. *J Adv Ceram* 2024, **13**: 354–363.
[52] Qin X, Liu XW, Huang W, *et al.* Lanthanide-activated phosphors based on 4f–5d optical transitions: Theoretical and experimental aspects. *Chem Rev* 2017, **117**: 4488–4527.
[53] Lin YC, Bettinelli M, Karlsson M. Unraveling the mechanisms of thermal quenching of luminescence in Ce^{3+}-doped garnet phosphors. *Chem Mater* 2019, **31**: 3851–3862.
[54] Blasse G. Energy transfer in oxidic phosphors. *Phys Lett A* 1968, **28**: 444–445.
[55] Dai QL, Song HW, Wang MY, *et al.* Size and concentration effects on the photoluminescence of La_2O_2S:Eu^{3+} nanocrystals. *J Phys Chem C* 2008, **112**: 19399–19404.
[56] Lin YC, Bettinelli M, Sharma SK, *et al.* Unraveling the impact of different thermal quenching routes on the luminescence efficiency of the $Y_3Al_5O_{12}$:Ce^{3+} phosphor for white light emitting diodes. *J Mater Chem C* 2020, **8**: 14015–14027.
[57] Tian QX, Zhang Y, Wang Z, *et al.* Novel phosphors Co-doped with Tb^{3+}/Mn^{4+} for green-red emissions modulation and anti-counterfeiting applications. *Ceram Int* 2025, **51**: 36904–36911.
[58] Chen XR, Yuan SD, Liu BG, *et al.* Unveiling the effect of Ce^{3+} doping concentration in YAG:Ce single crystals towards high luminance laser lighting. *J Lumin* 2024, **275**: 120786.
[59] Sun P, Hu P, Liu YF, *et al.* Luminescence-refrigeration module: Addressing luminescence saturation challenges in laser-driven lighting. *Laser Photonics Rev* 2024, **18**: 2300969.
[60] Lin SS, Lin H, Huang QM, *et al.* Highly crystalline $Y_3Al_5O_{12}$:Ce^{3+} phosphor-in-glass film: A new composite color converter for next-generation high-brightness laser-driven lightings. *Laser Photonics Rev* 2022, **16**: 2200523.
[61] Garshasbi S, Huang SJ, Valenta J, *et al.* Enhancing the cooling potential of photoluminescent materials through evaluation of thermal and transmission loss mechanisms. *Sci Rep-UK* 2021, **11**: 14725.
[62] Li ZW, Zhu G, Li SS, *et al.* Ultra-small Stokes shift induced thermal robust efficient blue-emitting alkaline phosphate phosphors for LWUV WLEDs. *Ceram Int* 2023, **49**: 21510–21520.